

Optical model potentials involving loosely bound p -shell nuclei around 10 MeV/nucleon

L. Trache, A. Azhari, H. L. Clark, C. A. Gagliardi, Y.-W. Lui, A. M. Mukhamedzhanov, and R. E. Tribble
Cyclotron Institute, Texas A&M University, College Station, Texas 77843

F. Carstoiu

Institute of Atomic Physics, P.O. Box MG-6, Bucharest, Romania

(Received 25 August 1999; published 20 January 2000)

We present the results of a search for optical model potentials for use in the description of elastic scattering and transfer reactions involving stable and radioactive p -shell nuclei. This was done in connection with our program to use transfer reactions to obtain data for nuclear astrophysics, in particular for the determination of the astrophysical S_{17} factor for ${}^7\text{Be}(p, \gamma){}^8\text{B}$ using two (${}^7\text{Be}, {}^8\text{B}$) proton transfer reactions. Elastic scattering was measured using ${}^7\text{Li}$, ${}^{10}\text{B}$, ${}^{13}\text{C}$, and ${}^{14}\text{N}$ projectiles on ${}^9\text{Be}$ and ${}^{13}\text{C}$ targets at or about $E/A = 10$ MeV/nucleon. Woods-Saxon type optical model potentials were extracted and are compared with potentials obtained from a microscopic double folding model. Several nucleon-nucleon effective interactions were used: M3Y with zero range and finite range exchange term, two density dependent versions of M3Y and the effective interaction of Jeukenne, Lejeune, and Mahaux. We find that the latter one, which has an independent imaginary part, gives the best description. Furthermore, we find the renormalization constant for the real part of the folding potential to be nearly independent of the projectile-target combination at this energy and that no renormalization is needed for the imaginary part. From this analysis, we are able to eliminate an ambiguity in optical model parameters and thus better determine the asymptotic normalization coefficient for ${}^{10}\text{B} \rightarrow {}^9\text{B} + p$. Finally we use these results to find optical model potentials for unstable nuclei with emphasis on the reliability of the description they provide for peripheral proton transfer reactions. We discuss the uncertainty introduced by the procedure in the prediction of the distorted wave Born approximation cross sections for the (${}^7\text{Be}, {}^8\text{B}$) reactions used in extracting the astrophysical factor $S_{17}(0)$.

PACS number(s): 25.70.Bc, 24.10.Ht, 25.70.Hi, 27.20.+n

I. INTRODUCTION

Transfer reactions have been proposed as an indirect method to determine direct capture reaction rates at stellar temperatures for some time [1–3]. Recently we used the asymptotic normalization coefficient (ANC) method to determine the cross section for the radiative proton capture process ${}^7\text{Be}(p, \gamma){}^8\text{B}$ at solar energies, or equivalently, the astrophysical factor, $S_{17}(0)$. The method relies on the fact that at low energies a capture reaction to a loosely bound state is a surface process. Its cross section is determined by the tail of the radial overlap integral between the bound state wave function of the final nucleus and those of the initial colliding nuclei. This overlap integral is asymptotically proportional to a well-known Whittaker function, and therefore the knowledge of its asymptotic normalization alone determines the cross section. This asymptotic normalization, in turn, can be determined from the measurement of a transfer reaction involving the same vertex, provided that this second reaction is also peripheral. In particular, we determined $S_{17}(0)$ from measurements of the ANC for the ${}^8\text{B} \rightarrow {}^7\text{Be} + p$ system utilizing the proton transfer reactions ${}^{10}\text{B}({}^7\text{Be}, {}^8\text{B}){}^9\text{Be}$ [4] and ${}^{14}\text{N}({}^7\text{Be}, {}^8\text{B}){}^{13}\text{C}$ [5], at energies where the proton transfer process is peripheral. Determining the ANCs from transfer reactions involves distorted wave Born approximation (DWBA) calculations, and therefore good, reliable optical potentials are needed. In particular, good optical model potentials are needed in both the initial and the final channels involving ${}^7\text{Be}$ and ${}^8\text{B}$ radioactive nuclei in each reaction in order to compute the DWBA proton transfer cross sections.

For example, recent attempts to infer the ANC for ${}^8\text{B} \rightarrow {}^7\text{Be} + p$ from $d({}^7\text{Be}, {}^8\text{B})n$ measurements [6,7] have been shown to have substantial ambiguities due to uncertainties in the optical model potentials [8,9]. Because elastic scattering data with these projectiles cannot be easily obtained and/or are not precise enough to extract reliable and unambiguous optical potentials, we have studied elastic scattering for several combinations of p -shell nuclei at energies close to those appearing in the reactions of interest. We then determine procedures to extract optical model potentials for the cases involving radioactive partners.

Angular distributions up to the nuclear rainbow angle were measured in seven experiments using ${}^7\text{Li}$, ${}^{10}\text{B}$, ${}^{13}\text{C}$, and ${}^{14}\text{N}$ projectiles on ${}^9\text{Be}$ and ${}^{13}\text{C}$ targets at bombarding energies at or around $E/A = 10$ MeV/nucleon. They were fitted with phenomenological potentials with volume Woods-Saxon real and imaginary terms. The phenomenological optical model potentials found for all systems were then compared with the potentials calculated with microscopic double folding procedures, using six effective nucleon-nucleon interactions: M3Y with zero range and finite exchange term, the density dependent M3Y interaction in the forms extracted recently by Khoa *et al.* [10] (BDM3Y1, BDM3Y3) and the interaction of Jeukenne, Lejeune, and Mahaux (JLM) [11] in two versions. For the calculations, one-body densities were obtained in a standard spherical Hartree-Fock calculation using the density functional of Beiner and Lombard [12], with a slight modification of the surface term in order to fit the experimental binding energy for each nucleus. These densities were used in the double

folding procedure. The renormalization coefficients needed for the analysis of elastic data with these double folding potentials are extracted and discussed. The methods applied here—phenomenological Woods-Saxon potentials extracted from fits to elastic scattering data and semimicroscopic potentials derived from folding effective NN interactions with nuclear densities—have a long history of systematic application for $1p$ -shell nuclei, but they have not been thoroughly checked for nuclei with very loosely bound clusters or nucleons (such as halo or Borromean nuclei). There is an alternative microscopic approach for deriving the optical potential when one of the partners is a loosely bound nucleus. This involves solving Faddeev-type equations, modified to account for the composition of the colliding particles, since the constituent fragments are not nucleons. This can be done by including antisymmetrization and excluding Pauli-forbidden states through a modification of the input interaction potentials in the Faddeev equations. The Alt-Grassberger-Sandhas equations [13], which are a quasi-two-particle modification of the Faddeev equations, are suitable for this purpose. Although this approach is very promising in our energy regime, around 10 MeV/nucleon, no calculations have been performed for loosely bound nuclei, mainly because of the complexity of the problem and the attendant computational difficulties. At higher energies (several hundred MeV per nucleon), a simplified version of the few-body approach has been used [14] which utilizes an S matrix of the Glauber form describing the interaction of the constituent fragments of a loosely bound projectile with a target and few-body wave functions of the projectile. Since we are working at significantly lower energies than those appropriate to the Glauber model, we chose to use microscopic folding potentials which are also well suited for DWBA calculations of transfer reactions.

In two cases the elastic scattering data were also used to extract the parameters of the optical model potentials that were needed for DWBA calculations to determine the ANC for the $^{10}\text{B} \rightarrow ^9\text{Be} + p$ and $^{14}\text{N} \rightarrow ^{13}\text{C} + p$ systems from the $^9\text{Be}(^{10}\text{B}, ^9\text{Be})^{10}\text{B}$ [15] and $^{13}\text{C}(^{14}\text{N}, ^{13}\text{C})^{14}\text{N}$ [16] reactions, respectively, and were included in those publications. These measurements also allowed us to test the results of our folding procedures for the proton transfer reactions by comparing the results of the DWBA calculations that we obtain from the double folding model potentials with those we obtain using the phenomenological potentials. From the analysis presented below, we are able to eliminate the uncertainty in the optical potentials found in Ref. [15]. This results in a better determination of the ANC for $^{10}\text{B} \rightarrow ^9\text{Be} + p$. We chose the elastic scattering of ^7Li on both targets as being close to what we expect for the scattering of ^7Be . Both ^7Li and ^7Be nuclei have low binding energies and large break-up probabilities. The elastic scattering of ^{13}C on the ^9Be target was studied as this is close to the exit channel $^{13}\text{C} + ^8\text{B}$ of the second proton transfer reaction $^{14}\text{N}(^7\text{Be}, ^8\text{B})^{13}\text{C}$.

The double folding procedure and the parameters extracted for the effective nucleon-nucleon interaction from the present experimental data were also checked for other projectile-target combinations in the same mass and energy region for which data exist in the literature. The results were

TABLE I. List of the elastic scattering experiments presented in this paper.

No.	Projectile-target	E (MeV)	θ_{lab} (deg.)
1	$^{10}\text{B} + ^9\text{Be}$	100	4–30
2	$^{13}\text{C} + ^9\text{Be}$	130	4–22
3	$^{14}\text{N} + ^{13}\text{C}$	162	2–34
4	$^7\text{Li} + ^9\text{Be}$	63	4–52
5	$^7\text{Li} + ^{13}\text{C}$	63	4–56
6	$^7\text{Li} + ^9\text{Be}$	130	4–47
7	$^7\text{Li} + ^{13}\text{C}$	130	4–47

in agreement with those found from the study of the seven cases described here. Using the techniques developed here, we calculated the optical model parameters required to extract the ANC for the $^7\text{Be} + p \rightarrow ^8\text{B}$ system, and consequently $S_{17}(0)$, from the studies of the $^{10}\text{B}(^7\text{Be}, ^8\text{B})^9\text{Be}$ [4] and $^{14}\text{N}(^7\text{Be}, ^8\text{B})^{13}\text{C}$ [5] reactions. Section II presents the experiments and the procedures used in the data reduction. We extract the Woods-Saxon optical model potentials from fits to the elastic scattering data in Sec. III, and compare them with those microscopically calculated in Sec. IV. In Secs. V and VI, we describe a global optical potential for interactions involving loosely bound p -shell nuclei and its implications for the $^{10}\text{B}(^7\text{Be}, ^8\text{B})^9\text{Be}$ and $^{14}\text{N}(^7\text{Be}, ^8\text{B})^{13}\text{C}$ reactions. Finally, Sec. VI presents the conclusions.

II. THE EXPERIMENTS

The experiments were carried out using beams from the Texas A&M University K500 superconducting cyclotron. A list of the measurements is given in Table I. The experimental setup and the data reduction procedures were similar to those already described in Ref. [15]. The multipole-dipole-multipole (MDM) magnetic spectrometer [17] was used to analyze the scattered particles and the reaction products. The beams were prepared using the beam analysis system [18], which allows for the control of the energy and angular spread of the beam. Self-supported ^9Be and ^{13}C targets, about 200–300 $\mu\text{g}/\text{cm}^2$ thick, obtained by evaporation, were placed perpendicular to the beam in the sliding-seal target chamber of the MDM. The magnetic field of the spectrometer was set to transport fully stripped ions to its focal plane, where they were observed in the modified Oxford detector [19]. There, the position of the particles along the dispersive direction was measured with resistive wires at four different depths within the detector, separated by about 16 cm each. For particle identification we used the specific energy loss measured in the ionization chamber and the residual energy measured in a NE102A plastic scintillator located in air, just behind the output window of the detector. The input and output windows of the detector were made of 1.8 and 7.2 mg/cm^2 thick Kapton foils, respectively. The ionization chamber was filled with pure isobutane at pressures between 30–50 Torr. The entire horizontal acceptance of the spectrometer, $\Delta\theta = \pm 2^\circ$, and a restricted vertical opening, $\Delta\phi = \pm 0.5^\circ$, were used in these measurements. Raytracing was used to reconstruct the scattering angle in the analysis of the data.

For this purpose, in addition to RAYTRACE [20] calculations, angle calibration data were obtained at several angles by using an angle mask consisting of five openings of $\delta\theta=0.1^\circ$, located at -1.6° , -0.8° , 0° , $+0.8^\circ$, and $+1.6^\circ$ relative to the central angle of the spectrometer. Moving the spectrometer from $\theta_{\text{lab}}=4^\circ$ to 54° we covered the angular ranges listed in Table I. Typically we moved the spectrometer by 2° or 3° at a time, allowing for an angle overlap that provided a self-consistency check of the data at all angles. Normalization of the data was done using current integration in a Faraday cup. Focal plane reconstruction was done at each angle using the position measured with the signals in the wire nearest to the focal plane and using the detector angle obtained from the position measured at two of the four wires. The angular range of $\Delta\theta=4^\circ$ covered by the acceptance slit was divided into eight bins, resulting in eight points in the angular distribution being measured simultaneously, with each integrating over $\delta\theta_{\text{lab}}=0.5^\circ$.

The measurements with the angle mask showed that the resolution in the scattering angle (laboratory) was $\Delta\theta_{\text{res}}=0.20^\circ-0.25^\circ$ full-width at half maximum (FWHM). This includes a contribution from the angular spread of the beam of about 0.1° . The best energy resolution obtained at forward angles was 150 keV FWHM for ^{10}B on ^9Be , 230 keV for ^{14}N on ^{13}C and 150 and 220 keV for the scattering of ^7Li at 63 MeV and 130 MeV, respectively. It degraded as we advanced to larger angles due to the large kinematic factor, $k=(1/p)(dp/d\theta)$, coupled with the finite angular spread in the beam. However, it never degraded our ability to isolate the elastic peak, even in the most demanding case of the ^7Li experiments where the first excited state of the projectile is only 477 keV away. A sample spectrum taken in one of these most demanding cases, ^7Li (130 MeV) + ^9Be , is presented in Fig. 1 where the good separation is clear. The active length of the focal plane allowed us to cover a total excitation energy of about 7 MeV, centered around the elastic peak. Thus we were able to measure inelastic scattering to the lowest excited states of the projectile-target systems at the same time. These inelastic scattering data were used as additional information to check the experimental procedures, and in a few cases we compared the inelastic transition strength obtained in these experiments (deformation parameters or deformation lengths) with those available in literature.

During the experiments, particular emphasis was placed on obtaining accurate absolute values for the cross sections, and therefore target thickness and charge collection factors were determined by a two-target method and by normalization to Rutherford scattering at forward-most angles, as described in Ref. [15]. Combining the results of these independent determinations, we conclude that we have an overall normalization accuracy of 7% for the absolute values of the cross sections for both the elastic scattering $^9\text{Be}(^{10}\text{B}, ^{10}\text{B})^9\text{Be}$ data and for the proton transfer $^9\text{Be}(^{10}\text{B}, ^9\text{Be})^{10}\text{B}$ data [15] and for the elastic scattering $^{13}\text{C}(^{14}\text{N}, ^{14}\text{N})^{13}\text{C}$ and proton transfer reaction $^{13}\text{C}(^{14}\text{N}, ^{13}\text{C})^{14}\text{N}$ [16]. The normalization for the absolute values of the cross section was made in the ^{13}C (130 MeV) + ^9Be case only using the nine most forward

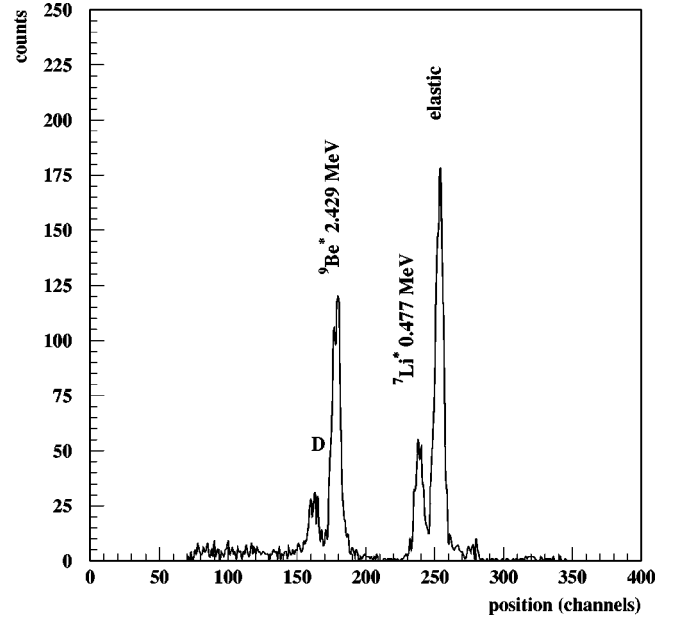


FIG. 1. Spectrum from the elastic scattering of ^7Li on the ^9Be target at $E_{\text{lab}}=130$ MeV and $\theta_{\text{lab}}=27.25^\circ \pm 0.25^\circ$. The peak labeled D is a combination of inelastic excitation of ^9Be (2.9 MeV) and of double excitation of the target and projectile.

angle data points in the angular distribution and is estimated to be accurate to 10%. For the experiments with the ^7Li beam, we also determined the target thickness by measuring the energy loss of α particles from a ^{228}Th source and the accuracy in normalization is 9%.

III. PHENOMENOLOGICAL ANALYSIS

The elastic scattering data have been fitted using the code OPTIMINIX [21] in a standard optical model analysis using volume Woods-Saxon form factors with the standard notation

$$U(r) = -[Vf_v(r) + iWf_w(r)], \quad (1)$$

where

$$f_x(r) = \left[1 + \exp\left(\frac{r - r_x(A_1^{1/3} + A_2^{1/3})}{a_x}\right) \right]^{-1}, \quad (2)$$

and $x=V, W$ stands for the real and imaginary parts of the potentials, respectively. Fits using the codes PTOLEMY [22] and ECIS [23] gave similar results. Only the central components have been included in the optical potential, since vector and higher rank tensor spin-orbit couplings have little or no influence on the cross sections.

In Fig. 2 we present the angular distributions measured for $^{10}\text{B}+^9\text{Be}$ at $E(^{10}\text{B})=100$ MeV, $^{14}\text{N}+^{13}\text{C}$ at $E(^{14}\text{N})=162$ MeV and $^{13}\text{C}+^9\text{Be}$ at $E(^{13}\text{C})=130$ MeV and in Fig. 3 those for $^7\text{Li}+^9\text{Be}$, ^{13}C at $E(^7\text{Li})=63$ and 130 MeV. All angular distributions display typical patterns for elastic scattering, dominated by strong absorption with Fraunhofer oscillations of large amplitude around the crossing point, followed by less developed structures at larger angles. The

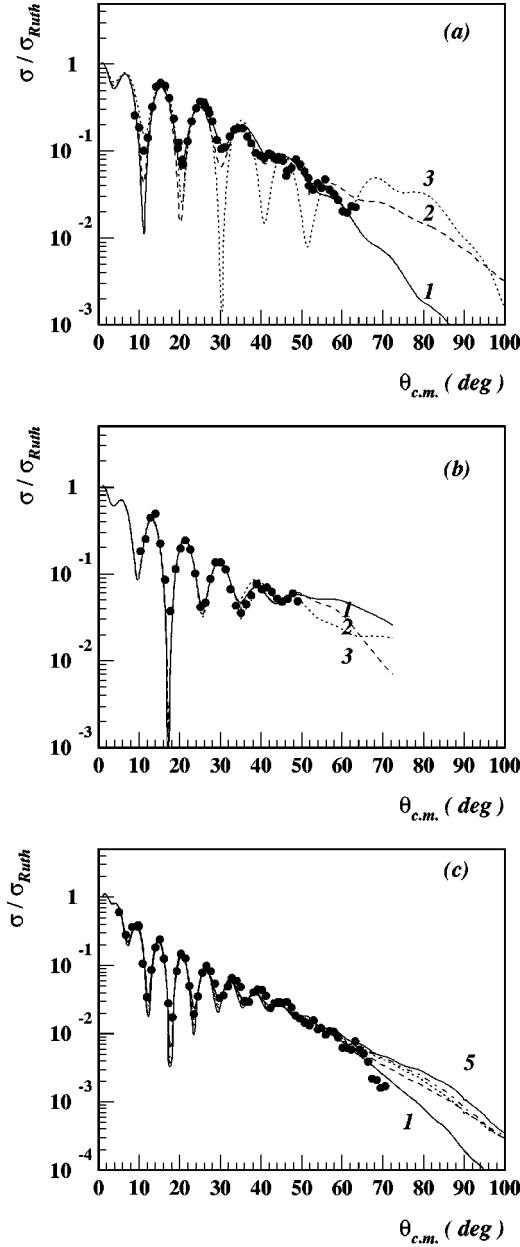


FIG. 2. Angular distributions for the elastic scattering of (a) ^{10}B (100 MeV) + ^9Be , (b) ^{13}C (130 MeV) + ^9Be , and (c) ^{14}N (162 MeV) + ^{13}C . The curves are fits with the potentials presented in Table II.

Fraunhofer oscillations are expected for such systems, due to the small Sommerfeld parameter $\eta \approx 1$. The curves are the fits to the data. Inspecting Figs. 2 and 3, one observes that all potentials predict somewhat deeper minima than the data show. This effect is partially attributable to the finite angular resolution. The rest is probably due to the incoherent contribution of the substantial quadrupole moment of some of the partners (such as ^9Be). During the normalization procedure, the theoretical curves were convoluted with the experimental angular resolution and binning, using the code ECIS, but this was found to have no influence on the fits.

The optical model parameters extracted for all seven cases studied here are presented in Table II. In addition to the

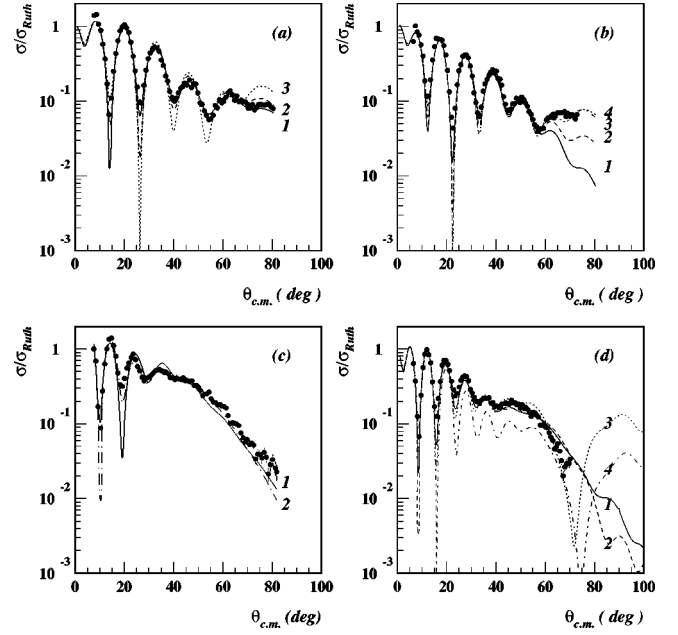


FIG. 3. Same as Fig. 2, for the systems (a) ^7Li (63 MeV) + ^9Be , (b) ^7Li (63 MeV) + ^{13}C , (c) ^7Li (130 MeV) + ^9Be , and (d) ^7Li (130 MeV) + ^{13}C .

depth, reduced radius and diffuseness for the real and imaginary parts of the potential, the table gives the reduced chi-square for the fit (χ^2_ν), the total reaction cross section (σ_R), the values of the volume integrals per pair of interacting nucleons for the real (J_V) and imaginary parts (J_W) of the potential, respectively, and the root-mean-square radii of the real (R_V) and imaginary (R_W) potentials. The parameters were obtained by gridding the initial strength of the real potential in small steps in the range $V = 50\text{--}250$ MeV in order to identify the local minima and then searching for minima on all parameters with no constraints. In this way 3–4 families of potentials have been found for each case. Usually, a characteristic jump of $50\text{--}70$ MeV fm 3 in the volume integral of the real part of the optical potential serves to identify these potentials as discrete members of a sequence of potentials which give a comparable description of the data. The members of each family of potentials are connected by the well known continuous Igo ambiguity $V \exp(R_V/a_V) = \text{const}$ [24]. This arises since, due to the strong absorption, the cross section is sensitive only to the tail of the potential. The Igo potentials of the same family have practically the same volume integral and the same radius and therefore the discrete families of potentials can be identified by the values of these parameters. The absorption is seen to be independent of the strength and shape of the real part of the optical potential and, as a consequence, the reaction cross section is more or less constant along the sequence in each case. Also we notice that generally the radii of the imaginary potentials are about 20% larger than those for the real potentials, in agreement with previous observations [25].

For the $^{10}\text{B} + ^9\text{Be}$ case, it appears that potential 1, which has the smallest chi-square, provides the most realistic description, and potential 3 can be rejected. In the angular range covered, the prediction of potential 2 for the elastic

TABLE II. The parameters of the Woods-Saxon optical model potentials extracted from the analysis of the elastic scattering data for projectile-target combinations studied here. $r_C=1$ fm for all potentials.

Channel	Pot.	V [MeV]	W [MeV]	r_V [fm]	r_W [fm]	a_V [fm]	a_W [fm]	χ^2_ν	σ_R [mb]	J_V [MeV fm ³]	R_V [fm]	J_W [MeV fm ³]	R_W [fm]
¹⁰ B (100 MeV)+ ⁹ Be	1	64.2	30.1	0.78	0.99	0.99	0.75	19.8	1318	206	4.51	136	4.28
	2	131.2	29.7	0.67	0.95	0.90	0.86	45.4	1411	276	3.99	131	4.46
	3	203.2	24.7	0.81	1.04	0.60	0.83	61.8	1428	499	3.46	133	4.59
¹⁴ N (162 MeV)+ ¹³ C	1	79.22	30.27	0.96	1.05	0.76	0.72	17.4	1542	221	4.52	105	4.69
	2	134.76	35.23	0.88	1.05	0.75	0.67	18.3	1525	299	4.28	120	4.61
	3	176.03	35.84	0.86	1.07	0.72	0.65	23.3	1527	361	4.15	125	4.62
	4	241.36	37.45	0.82	1.06	0.71	0.66	27.5	1533	438	4.00	129	4.61
	5	306.44	39.14	0.81	1.05	0.68	0.68	36.1	1552	522	3.90	132	4.61
¹³ C (130 MeV)+ ⁹ Be	1	94.2	20.9	0.77	0.99	0.87	0.97	15.0	1592	223	4.19	94	4.96
	2	164.2	23.0	0.67	0.98	0.86	0.95	14.2	1576	283	3.94	99	4.87
	3	226.7	31.9	0.62	0.90	0.85	0.95	14.8	1573	328	3.81	113	4.70
⁷ Li (63 MeV)+ ⁹ Be	1	134.4	19.82	0.54	1.03	0.95	0.92	8.0	1414	267	3.90	137	4.66
	2	221.6	27.33	0.54	0.92	0.83	0.97	10.6	1449	367	3.50	153	4.60
	3	276.5	37.3	0.61	0.81	0.72	1.02	15.7	1482	499	3.27	158	4.64
⁷ Li (63 MeV)+ ¹³ C	1	54.3	29.9	0.92	1.03	0.79	0.69	28.8	1318	209	4.21	144	4.26
	2	99.8	22.0	0.77	1.01	0.81	0.81	21.6	1363	257	3.92	109	4.49
	3	154.8	22.7	0.76	1.00	0.71	0.83	19.8	1378	357	3.64	111	4.51
	4	244.6	26.4	0.68	0.96	0.71	0.84	20.4	1382	438	3.47	117	4.45
⁷ Li (130 MeV)+ ⁹ Be	1	60.0	17.71	0.86	1.07	0.65	1.12	150.	1564	217	3.58	154	5.33
	2	129.4	30.7	0.57	0.80	0.90	1.17	208	1488	261	3.77	158	5.02
⁷ Li (130 MeV)+ ¹³ C	1	123.3	32.74	0.76	0.94	0.76	0.90	79.1	1406	297	3.79	145	4.66
	2	157.9	31.97	0.63	0.90	0.87	0.94	77.3	1393	289	3.83	133	4.59
	3	201.9	25.59	0.73	1.03	0.69	0.86	129.	1418	419	3.52	142	4.66
	4	300.0	30.78	0.73	0.98	0.64	0.89	147.	1441	543	3.37	150	4.63

scattering differs from that of potential 1 primarily in the depths of its minima. We reached the same conclusion from the comparison of the DWBA calculations for the proton transfer reaction ${}^9\text{Be}({}^{10}\text{B}, {}^9\text{Be}){}^{10}\text{B}$ studied in the same experiment: whereas potentials 1 and 2 give a very good description of the shape of the angular distribution and similar absolute values, potential 3 predicts a reaction cross section which is far too small [15]. To further clarify the features of the angular distribution we have performed a near-far decomposition of the scattering amplitude, with one potential taken as the reference potential. Shown in Fig. 4(a) are the cross sections due to the near-side and far-side components of the total scattering amplitude. Around the crossing angle of $\theta_{\text{c.m.}}=16^\circ$, the strong interference between the near- and far-side components results in Fraunhofer oscillations of large amplitude. Beyond this angle, the near-side component drops rapidly and the angular distribution is dominated by the far-side component, which falls off smoothly. No significant structure could be identified in this region. This structureless behavior can be understood qualitatively in terms of the transparency for the low partial waves implied by the refractive potential. In the case of ${}^{10}\text{B}+{}^9\text{Be}$, the rainbow partial wave has $l_R=16$ and the associated scattering matrix elements are of the order $|S_l|\approx 3\times 10^{-3}$ for $l\ll l_R$. Thus, the refractive nature of the potential is sufficient to allow the interference between waves with $l<16$ and higher ones to produce the smooth behavior. Comparison of the potential

elastic scattering branch (forward angles) and of the elastic proton exchange branch (backward angles) in Fig. 3 of Ref. [15] shows that the interference between these two mechanisms has no sizable effect in the angle range considered here and was not considered in the analysis. The data for the ${}^{13}\text{C}({}^{130}\text{MeV})+{}^9\text{Be}$ experiment show similar features, with three families of potentials found.

For the ${}^{14}\text{N}+{}^{13}\text{C}$ system the volume integral and radius for the absorptive part of the optical potential seems to be independent of the real potential, resulting in a constant total reaction cross section along the sequence with an average value of 1535 mb. The optical model total reaction cross section is consistent with the experimental value measured by DiGregorio *et al.* at 161.3 MeV, $\sigma=1463\pm 100$ mb [26]. All potentials give reasonable χ^2 , but potential 1 listed in the table gives the smallest value and is the only one that fits the data at the largest angles. This potential has a volume integral per pair of interacting nucleons close to that which we found for ${}^{10}\text{B}+{}^9\text{Be}$ elastic scattering at similar velocities. Potential 1 was adopted for the DWBA calculation of the proton exchange process ${}^{13}\text{C}({}^{14}\text{N}, {}^{13}\text{C}){}^{14}\text{N}$ as described in Ref. [16], while the others were used to estimate the uncertainty due to the choice of optical model parameters. Similar insight on the relative role played by the refractive and absorptive parts of the optical potential may be obtained from the far side-near side decomposition of the scattering amplitude corresponding to potential 1 which is presented in Fig.

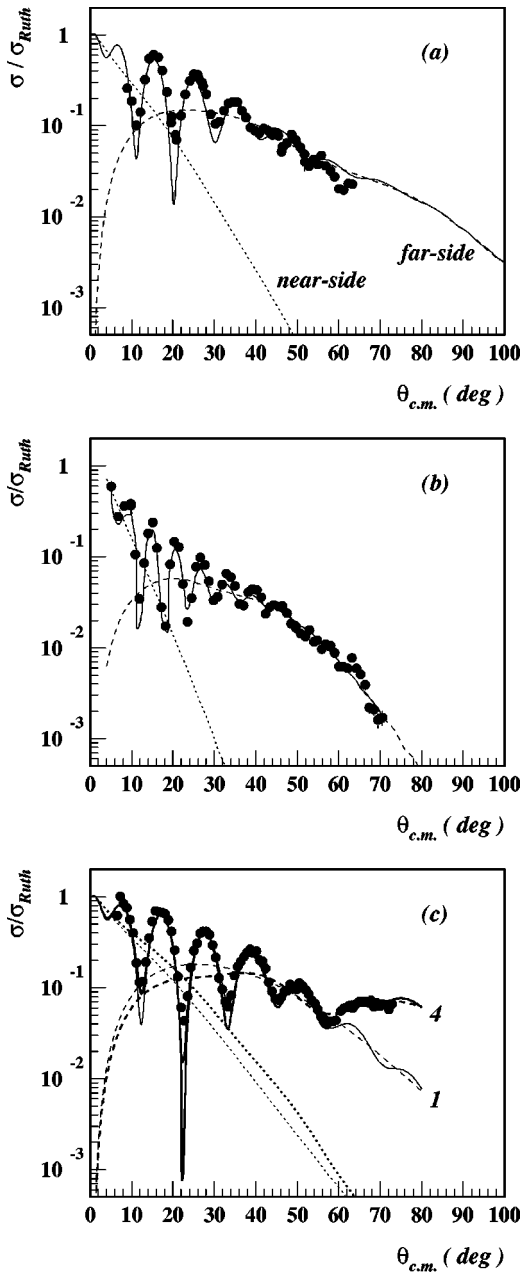


FIG. 4. The near-side/far-side decomposition of the elastic scattering for (a) $^{10}\text{B} + ^9\text{Be}$, (b) $^{14}\text{N} + ^{13}\text{C}$, and (c) ^7Li (63 MeV) + ^{13}C .

4(b). The far-side component is represented by the dashed line and the near-side component by the dotted line and their coherent sum by the continuous line. For angles around the crossing where the two components have comparable amplitude and strongly interfere, a typical Fraunhofer diffraction pattern emerges with large amplitude oscillations equally spaced by $\Delta\theta = \pi/l_g = \pi/30$, where l_g is the grazing angular momentum. Beyond this angle, the near side component is completely damped by the strong absorption and we are left with the far side exponential tail that is characteristic of far-side dominance. No significant structure could be identified up to the nuclear rainbow angle, which in this case is $\theta_R = 83^\circ$. Similar to the case of the $^{10}\text{B} + ^9\text{Be}$ experiment, our

measurements show that we do not have interference effects between the potential scattering predominant at forward angles and the elastic proton exchange predominant at backward angles (see Fig. 2 of Ref. [16]) in the angular range considered.

The potentials found in the phenomenological WS analysis of ^7Li scattering are given in Table II. A similar result emerges, with discrete ambiguities represented by up to four families found in each case. Similar values are found for the volume integrals for the real and imaginary parts as for the rest of the cases studied above. We notice however that the reduced radii $r_{V,W}$ are small and the diffusivities $a_{V,W}$ of the potentials are unusually large. This agrees with findings in other analyses for such light systems. Figure 4(c) shows the far-side, near-side decomposition for the $^7\text{Li} + ^{13}\text{C}$ system at 63 MeV, with conclusions similar with those for the cases discussed above.

It is interesting to note that, for all but one of the cases shown in Table II, the first of the potentials always has a similar volume integral for the real part $J_V \approx 220 \text{ MeV fm}^3$, and that the imaginary potentials are independent of the real part, predicting the same total cross sections.

As mentioned above, the spin dependent components of the optical potential have been omitted. In the absence of any polarization data, exploratory calculations for the $^{10}\text{B} + ^9\text{Be}$ system, using the same vector spin-orbit term as for $^6\text{Li} + ^{12}\text{C}$ [27] at $E = 156 \text{ MeV}$, did not result in any noticeable effects on the elastic cross section in the measured angular range. The effect of that same term in the calculation of the proton transfer cross section $^9\text{Be}(^{10}\text{B}, ^9\text{Be})^{10}\text{B}$ was a change of less than 2%. In fact, it is known that for heavy ions the strength of the spin-orbit potential scales as $1/A$ as compared with the nucleon case. For several of the cases studied here, we also did a Fourier-Bessel analysis of the data, similar to that in Ref. [28], and found that the phenomenological Woods-Saxon shapes assumed in Eq. (2) are adequate.

IV. FOLDING MODEL ANALYSIS

In addition to the analysis with Woods-Saxon type potentials, the data have been analyzed in the framework of a semimicroscopic folding model. We followed a Hartree-Fock procedure to obtain the densities in the two partners, then used double folding with known nucleon-nucleon interactions. The wave functions and the densities for all nuclei involved were obtained in a standard spherical Hartree-Fock calculation using the energy density functional of Beiner and Lombard [12]. This functional describes nuclear matter and the bulk properties of finite nuclei well. In the calculations, the parameters of the surface terms were adjusted slightly in order to reproduce the experimental total binding energy. This is an important constraint on the calculation, especially for nuclei with small separation energies such as ^9Be and ^7Li . Usually this correction amounts to a few percent with respect to the original parameters and substantially improves the description of the single particle levels close to the Fermi level. The calculated binding energies and the rms radii that were obtained are given in Table III and compared with the experimental ones. A similar procedure has been used by

TABLE III. Radii and binding energies of the calculated Hartree-Fock one-body densities, compared with the experimental data. R_p , R_n , R_m , and R_{ch} stand for the root mean square radii of the calculated proton, neutron, mass and charge distributions, respectively, and R_{ch}^{exp} is the experimental charge rms. B is the binding energies.

Nucleus	R_p [fm]	R_n [fm]	R_m [fm]	R_{ch} [fm]	R_{ch}^{exp} [fm] Ref. [29]	B_{th} [MeV]	B_{exp} [MeV] Ref. [30]
^6Li	2.21	2.20	2.20	2.21	2.54(5)	31.929	31.994
^7Li	2.15	2.35	2.26	2.16	2.39(3)	39.234	39.244
^7Be	2.37	2.14	2.28	2.38	2.36(2) ^a	37.606	37.600
^8B	2.57	2.18	2.43	2.58	2.45(5) ^a	37.744	37.737
^9Be	2.26	2.39	2.33	2.29	2.50(9)	58.203	58.164
^{10}B	2.40	2.39	2.40	2.45	2.45(12)	64.631	64.750
^{12}C	2.44	2.43	2.44	2.49	2.47(2)	92.149	92.161
^{13}C	2.47	2.56	2.52	2.53	2.440(25)	97.135	97.108
^{14}N	2.58	2.57	2.57	2.64	2.58(2)	104.246	104.658

^aProton density rms radius obtained by Tanihata *et al.* [31] from interaction cross sections.

Hoshino *et al.* [32] to describe the structure of the ^{11}Be nucleus.

In the double folding procedure, we used a number of G -matrix effective nucleon-nucleon (NN) interactions. The first one is the well known M3Y interaction. Recall that the nucleus-nucleus potential in the double folding model is given by

$$V_{\text{fold}}(R) = \int d\vec{r}_1 d\vec{r}_2 \rho_1(r_1) \rho_2(r_2) v_{\text{eff}}(\vec{r}_1 + \vec{R} - \vec{r}_2), \quad (3)$$

where $\rho_{1,2}$ are the single particle densities, and the interaction operator is of the form

$$v_{\text{eff}}(r) = v_D(r) + P_{1,2}^{\text{ex}} v_{\text{ex}}(r)$$

where the direct and exchange parts are averaged over spin-isospin states and $P_{1,2}^{\text{ex}}$ is the knock-on exchange operator in coordinate space. We assumed, as usual, that the one nucleon exchange knock-on term, which involves the exchange between the interacting nucleons, is dominant with respect to all other exchange contributions. The parameters for the direct and exchange components of M3Y were taken from Ref. [33]. In the standard version [25], the isoscalar component of the interaction consists of a finite range direct term, supplemented by an energy dependent zero range pseudo-potential which simulates well the one nucleon knock-on contribution to the interaction. The small isovector component of the interaction has also been included in the calculation and the corresponding results are denoted by M3Y/ZR throughout the paper. A finite range version of the M3Y interaction was also used for some of the systems analyzed in this paper. The lack of any explicit density dependence in the effective interaction results in potentials that are too deep in the interior to reproduce correctly the rainbow features at large angles observed, e.g., in α scattering at higher energy [34]. This can

be corrected by making the effective NN interaction depend upon the density of the nuclear matter in which the interacting nucleons are immersed. The requirement that nuclear matter saturates ensures that this density dependence reduces the strength of the interaction as the density increases, weakening the folding potential in the interior while leaving the surface values practically unchanged. For our purpose we adopted more recent interactions called BDM3Y n ($n=1$ and 3) which have been shown to give a good description of light ion scattering in a wide range of incident energies [10]. These interactions are based upon a G matrix derived from the Reid soft core NN potential. They incorporate a linear ($n=1$) or cubic ($n=3$) density dependence with parameters adjusted to give saturation in nuclear matter at the correct density and binding energy. The two interactions give very different compressibilities for nuclear matter ($K=230$ MeV for $n=1$ and $K=475$ MeV for $n=3$) covering a broad range of equations of state. We note that at present $K_\infty=231 \pm 5$ MeV has experimental support [35], which would indicate a preference for BDM3Y1 in the description of heavy ion elastic scattering.

Also, we have used the G -matrix interaction of Jeukenne, Lejeune, and Mahaux (JLM) [11], which is obtained in a Brueckner-Hartree-Fock (BHF) approximation from the Reid soft-core nucleon-nucleon potential. This interaction is complex, energy and density-dependent and, therefore, provides simultaneously both real and imaginary parts of the optical potential. The interaction has been considered recently by Bauge, Delaroche, and Girod [36] in an extensive study of nucleon scattering on a wide range of target masses and incident energies. Some shortcomings of the original interaction were also corrected in Ref. [36]. For completeness, we describe below the main steps in the derivation of our potentials, taking into account the improvements recommended in Ref. [36].

The optical potential for a nucleon of energy E traversing nuclear matter of density ρ is written as

$$U_{NM}(\rho, E) = V_0(\rho, E) + \alpha \tau V_1(\rho, E) + i[W_0(\rho, E) + \alpha \tau W_1(\rho, E)], \quad (4)$$

where $\alpha = (\rho_n - \rho_p)/(\rho_n + \rho_p)$ and $\tau = \pm 1$ for neutrons and protons, respectively. Explicit expressions for various terms are

$$V_0(\rho, E) = \sum_{i,j=1}^3 a_{ij} \rho^i E^{j-1}, \quad (5)$$

$$W_0(\rho, E) = \left(1 + \frac{D}{[E - \epsilon_F(\rho)]^2} \right)^{-1} \sum_{i,j=1}^4 d_{ij} \rho^i E^{j-1}, \quad (6)$$

$$V_1(\rho, E) = \frac{\tilde{m}}{m} \text{Re} N(\rho, E), \quad (7)$$

$$W_1(\rho, E) = \frac{m}{m} \text{Im} N(\rho, E). \quad (8)$$

The matrix coefficients a_{ij} , d_{ij} , the Fermi energy ϵ_F , and the BHF expression of the auxiliary function $N(\rho, E)$ are given in Ref. [36]. The quantities \tilde{m}/m and \bar{m}/m are the k mass and the E mass, respectively, and represent a measure of the true nonlocality and the true energy dependence of the optical potential.

In applications for heavy ions we interpret the quantity

$$v_0(\rho, E) = [V_0(\rho, E) + iW_0(\rho, E)]/\rho \quad (9)$$

as the (complex) isoscalar, density- and energy-dependent NN effective interaction. The heavy ion potential is given then by the folding integral

$$V(R) = \int d\vec{r}_1 d\vec{r}_2 \rho_1(r_1) \rho_2(r_2) v_0(\rho, E) \delta(\vec{s}) \quad (10)$$

with $\vec{s} = \vec{r}_1 + \vec{R} - \vec{r}_2$. Similarly, the quantity

$$v_1(\rho, E) = [V_1(\rho, E) + iW_1(\rho, E)]/\rho \quad (11)$$

is interpreted as the (complex) isovector, density- and energy-dependent NN effective interaction. The corresponding heavy ion potentials are obtained from a folding integral similar to that in Eq. (10), replacing v_0 by v_1 and the single particle densities $\rho_{1,2}$ by the isovector densities $(\rho_n - \rho_p)_{1,2}$. Usually such terms have little influence in the total optical potential because the isovector densities are small for normal nuclei in the p shell; however, we have included them in the analysis since such terms can have some importance in the case of loosely bound nuclei with very different proton and neutron single particle densities. Two approximations for the local density have been used. The first of them reads

$$\rho = \left[\rho_1 \left(\vec{r}_1 + \frac{\vec{s}}{2} \right) \rho_2 \left(\vec{r}_2 - \frac{\vec{s}}{2} \right) \right]^{1/2}, \quad (12)$$

which amounts to an estimate of the local density as the geometric average of the individual single particle densities, each of them evaluated at the mid distance between the interacting nucleons. This approximation has been used by Campi and Sprung [37] in Hartree-Fock calculations with density-dependent forces. With this approximation, the local density never exceeds the saturation value for nuclear matter density ρ_0 . We remind the reader that the JLM effective interaction is defined only for density values satisfying $\rho \leq \rho_0$. Potentials obtained with the above approximation are labeled below as JLM(1). The second approximation for the local density uses the arithmetic average of the individual densities:

$$\rho = \frac{1}{2} \left[\rho_1 \left(\vec{r}_1 + \frac{\vec{s}}{2} \right) + \rho_2 \left(\vec{r}_2 - \frac{\vec{s}}{2} \right) \right]. \quad (13)$$

A similar approximation was used by the authors of Ref. [38] in their derivation of the density-dependent version of M3Y, except for the factor of $\frac{1}{2}$ in front of the parentheses which is introduced here in order to be consistent with the assumptions of the JLM model. Potentials calculated with this ap-

proximation are denoted by JLM(2). It has been shown by the authors of Refs. [11] and [36] that the local density approximation is substantially improved by replacing the δ function in integrals of the type (10) by finite range form factors of the Gaussian shape

$$g(\vec{s}) = \left(\frac{1}{t\sqrt{\pi}} \right)^3 e^{-s^2/t^2}. \quad (14)$$

Since the finite range form factors are normalized to 1, the volume integrals of the folding potentials are not affected, only the rms radii are increased, depending on the values one chooses for the range parameter t . Our phenomenological analysis shows clearly that the bulk of the elastic scattering experimental data require larger radii for the absorptive part of the heavy ion optical potentials as compared to the real part. Extensive numerical calculations with both versions of the JLM interaction showed that optimum values for the range parameters are $t_R = 1.2$ fm and $t_I = 1.75$ fm. A similar need for different radii of the imaginary and real parts of the optical potential has been emphasized recently by Satchler and Khoa [34]. Of course slightly improved fits could be obtained in each individual case by varying also the range parameters around these values. For example, our ${}^7\text{Li}$ data were better fitted with a larger t_I . However, finding such variations for individual data sets goes beyond the purpose of the present paper.

It is known that p -shell nuclei elastic scattering, some of which involve loosely bound nuclei, cannot be described successfully without a substantial renormalization of the folding form factor [39]. The strong coupling with breakup and neutron transfer channels is responsible for such an effect. The usual procedure to simulate the repulsive effect of the real part of the dynamic polarization potential [40] arising from such coupling is to introduce a multiplicative constant for the real folding form factor. In the folding model with *real* effective interactions the absorption is accounted for phenomenologically by adding an imaginary potential of the same shape as the real part

$$U(r) = (N_V + iN_W) V_{\text{fold}}(r), \quad (15)$$

whereas for the cases when the effective interaction also has an *imaginary* component, the renormalization is

$$U(r) = N_V V_{\text{fold}}(r) + iN_W W_{\text{fold}}(r). \quad (16)$$

The resulting potentials differ from the Woods-Saxon shape at small distances, but can be easily fitted with such forms in their surface region. We reanalyzed all our elastic scattering data using double folding potentials obtained with the six effective interactions outlined above. The renormalization constants N_V and N_W were further adjusted to fit the elastic scattering data using Eq. (15) in the case of M3Y and BDM3Y forces and Eq. (16) for the two versions of the JLM interactions. The results of the fits are shown in Figs. 5 and 6, and the parameters are displayed in Table IV. In general, fits of reasonable quality were obtained with all interactions. However, the JLM interaction not only gives the best fits as

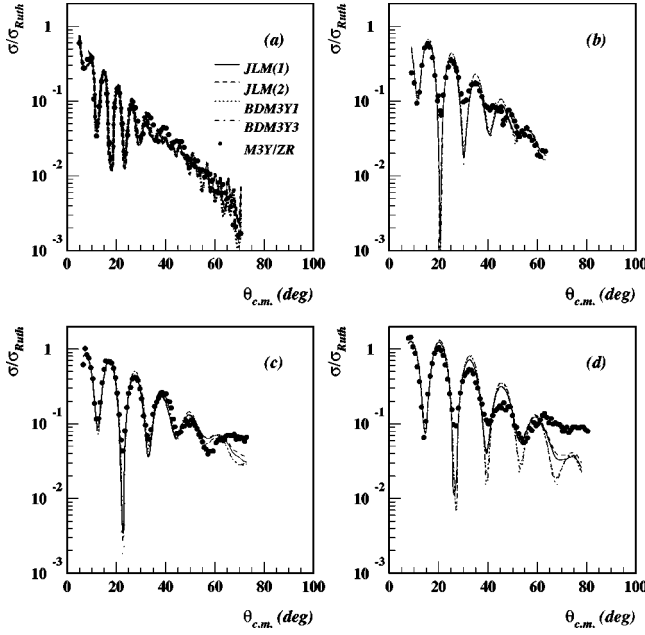


FIG. 5. Fit of the angular distributions with the folding potentials of Table IV. The curves are labeled: M3Y/ZR for the M3Y zero-range interaction, BDM3Y n for the density-dependent M3Y interactions, and JLM(n) for the interaction of Jeukenne, Lejeune, and Mahaux, respectively. The cases presented are (a) $^{14}\text{N} + ^{13}\text{C}$, (b) $^{10}\text{B} + ^9\text{Be}$, (c) $^7\text{Li}(63 \text{ MeV}) + ^{13}\text{C}$, and (d) $^7\text{Li}(63 \text{ MeV}) + ^9\text{Be}$.

compared to the other interactions, but also provides renormalization constants with minimal dispersion for all projectile-target combinations considered. This indicates that the mass dependence of the optical potential is properly taken into account by these effective interactions through the

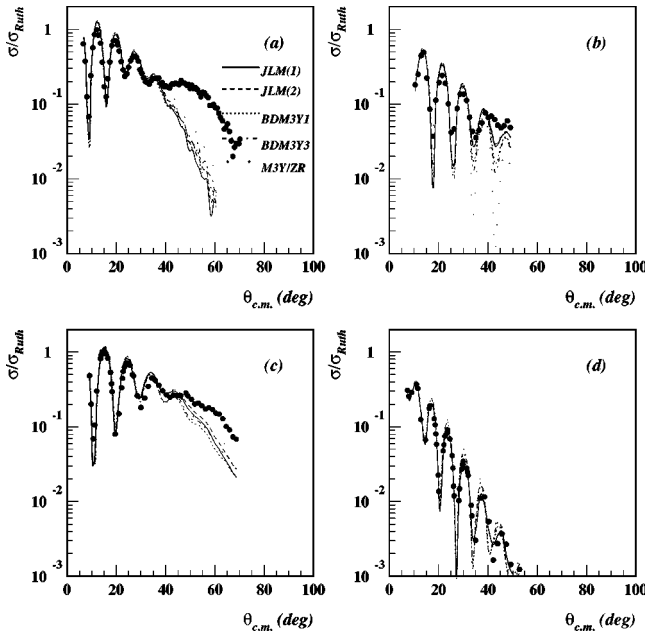


FIG. 6. Same as Fig. 5, but for the systems: (a) $^7\text{Li}(130 \text{ MeV}) + ^{13}\text{C}$, (b) $^{13}\text{C} + ^9\text{Be}$, (c) $^6\text{Li}(99 \text{ MeV}) + ^{12}\text{C}$, and (d) $^6\text{Li}(99 \text{ MeV}) + ^{28}\text{Si}$ (data from Ref. [41]).

density dependence. As a rule, all folding potentials need a substantial renormalization for the real part of the optical potential, emphasizing that the dynamic polarization potential plays an important role for p -shell nuclei elastic scattering at low energies. Density-dependent effects, such as those taken into account by BDM3Y forces, lead only to a slight increase in the real normalization constant N_V as compared to the original density-independent interaction M3Y/ZR, suggesting a need for a stronger density dependence at the potential surface. Inspecting Figs. 5 and 6 one sees that it is hard to distinguish between the two versions of this force since both of them give a comparable description of the data. This is likely a consequence of the fact that the present data give information on the optical potential in a limited spatial region centered around the strong absorption radius where the two do not differ much.

V. EXTRACTING A GLOBAL OPTICAL POTENTIAL

The analysis done as described in the previous section leads us to the conclusion that we can find a way to predict optical model potentials with some reliability. As already noted before, the situation is complicated by the fact that the nuclei involved are loosely bound and we expect to have important effects from break-up channels. Satchler and Love [25] concluded earlier that the renormalization of the real part of the double folding potentials is considerable, particularly for loosely bound nuclei where break-up is important. The energies studied here, around 10 MeV/nucleon, are known to lead to sizable effects due to the dynamic polarization contribution to the optical potential [34]. This is most likely the explanation behind the need for a substantially reduced real well depth. The renormalization coefficients are presented in Table IV and in Fig. 7 for both the real and imaginary part of the potentials. If we compare the results for the same nucleon-nucleon interaction, we see that similar renormalization constants are obtained for all systems when at least one of the participating nuclei is weakly bound. In particular when density-dependent effective interactions (JLM, BDM3Y1, BDM3Y3) are used, the renormalization constants are very stable, with a standard deviation of a few percent around the average value. This suggests that one can indeed obtain the optical model potentials for pairs of projectile-target nuclei for which data are not available, or are scarce, by using a folding procedure to obtain the geometrical parameters and the renormalization constants extracted above. Studies such as the one comparing the scattering of ^6Li and ^{11}Li lead to a similar conclusion, and show that the energy dependence in the potential is smooth and rather weak [42]. Furthermore, the renormalization factors that we find here are comparable to those found for $^6\text{Li} + ^{12}\text{C}$ near this energy when the M3Y and JLM interactions are used [42]. In a few cases the finite range version of the exchange term in the M3Y interaction was also checked but the results were not improved over those obtained with the zero range version of it. Given our suspicion that the localization procedure used to obtain these finite range calculations might not work properly in very light nuclei, we do not discuss the results here, but they are included in Table IV.

TABLE IV. Best fit renormalization parameters N_V and N_W for folding potentials with various effective interactions [see Eqs. (15) and (16)]. For each reaction channel, the values of N_V are given in the first line and N_W in the second line. For each effective interaction, the mean values and dispersions are given in the last two lines. Only cases 2–7 are used to determine averages, as described in the text.

No.	Projectile-target	JLM(1)	JLM(2)	M3Y/ZR	M3Y/FR	BDM3Y1	BDM3Y3
1	^{14}N (162 MeV) + ^{13}C	0.456	0.509	0.778	1.275	0.721	0.832
		0.844	0.996	0.469	0.887	0.419	0.492
2	^{10}B (100 MeV) + ^9Be	0.368	0.387	0.516	0.667	0.584	0.668
		1.168	1.131	0.571	1.116	0.506	0.596
3	^{13}C (130 MeV) + ^9Be	0.369	0.413	0.489		0.576	0.648
		0.937	1.124	0.726		0.550	0.656
4	^7Li (63 MeV) + ^{13}C	0.323	0.364	0.588	0.787	0.552	0.634
		1.00	1.007	0.503	0.831	0.458	0.535
5	^7Li (63 MeV) + ^9Be	0.360	0.403	0.588	0.759	0.568	0.645
		1.00	1.438	0.818	1.175	0.733	0.864
6	^7Li (130 MeV) + ^{13}C	0.380	0.418	0.595	0.914	0.571	0.651
		0.957	1.077	0.508	0.893	0.472	0.547
7	^7Li (130 MeV) + ^9Be	0.368	0.413	0.489	0.806	0.576	0.648
		0.937	1.124	0.726	1.110	0.550	0.656
8	^6Li (99 MeV) + ^{12}C	0.449	0.493	0.716	1.178	0.687	0.785
		1.044	1.166	0.536	0.942	0.510	0.585
9	^6Li (99 MeV) + ^{28}Si	0.368	0.408	0.565	0.960	0.534	0.611
		1.168	1.324	0.683	1.170	0.621	0.726
10	^7Li (63 MeV) + ^{12}C	0.278	0.309	0.502		0.478	0.546
		0.746	0.920	0.464		0.423	0.493
11	^7Li (79 MeV) + ^{12}C	0.315	0.347	0.521		0.505	0.573
		0.864	1.009	0.458		0.426	0.493
average of cases 2–7		0.366 ± 0.014	0.405 ± 0.017	0.553 ± 0.062	0.787 ± 0.089	0.578 ± 0.010	0.658 ± 0.013
		1.000 ± 0.087	1.143 ± 0.145	0.631 ± 0.131	1.025 ± 0.153	0.553 ± 0.082	0.631 ± 0.115

From all six effective nucleon-nucleon interactions used above, we favor the one denoted JLM(1) because it gives a slightly better fit than the others and the renormalization coefficients have the smallest spread around the average value (last rows in Table IV). In contrast to the real potential, no renormalization is needed for the imaginary part of the calculated potential, a sign that the imaginary part of the effective interaction and its density dependence are well accounted for. There might be a remaining slight dependence of the renormalization on energy, as found in other studies, but our data are insufficient to extract a definite conclusion on this dependence. However, it seems likely that most of the energy dependence is taken care of by the energy dependence of the effective interaction and by the density dependence used in the calculations. We also checked our double folding procedure on other systems than those mentioned above, and included the results in Table IV. Whereas we obtain very good fits to the data over a large mass and energy range, thus confirming the appropriateness of the JLM(1) effective interaction and of the smear function and ranges used in Eq. (14), the resulting renormalization coefficients, when using α particles for example, differ from those for the p -shell nuclei studied here and point to the conclusion that the present coefficients have only a local applicability. Analysis of α scattering of up to 60 MeV/nucleon on stable targets, lead to renormalization coefficients for the real part about a factor 2 larger. This is surely a reflection of the

differences between the very well bound ^4He nuclei and the loosely bound partners studied here. In order to obtain more complete information on the renormalization constants, we have included in our analysis two angular distributions involving the elastic scattering of another loosely bound p -shell nucleus ^6Li on light targets at 16 MeV/nucleon [41] and $^7\text{Li} + ^{12}\text{C}$ at two energies [43]. The volume integrals of the renormalized double folded potentials agree with the volume integrals of the first of the phenomenological potentials found and suggest that the phenomenological potentials with $J_V \approx 220 \text{ MeV fm}^3$ give the most realistic description.

Data in Fig. 7 and Table IV show that the renormalization coefficient of the real potential calculated with the JLM(1) interaction is somewhat higher for $^{14}\text{N} + ^{13}\text{C}$ than the average of the remaining 6 cases measured here. This is the only projectile-target combination where both nuclei are well bound, thus we should expect a smaller contribution from the polarization potential. The averages and standard deviations for all 7 cases are $N_V = 0.378 \pm 0.034$ (or 9%) and $N_W = 1.004 \pm 0.135$ (13%), respectively. Excluding the $^{14}\text{N} + ^{13}\text{C}$ system we find the averages $N_V = 0.366 \pm 0.014$ (or 4%) and $N_W = 1.000 \pm 0.087$ (9%). We see that the value of the renormalization coefficient is very stable. We suspect that a large part of the spread around the average of the renormalization coefficient for the imaginary potential comes from the uncertainties in the absolute normalization of our

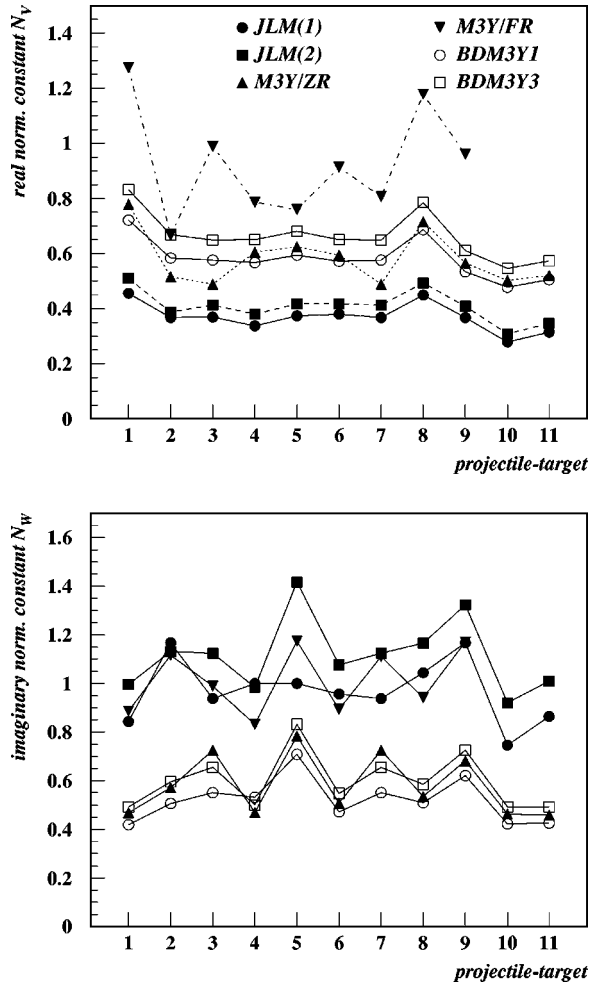


FIG. 7. The renormalization coefficients extracted for the double folding potentials calculated with the six effective nucleon-nucleon interactions, as described in the text. The projectile-target combinations are those of Table IV.

data. The real part of the potential, which is fixed mostly by the position of the oscillations in the angular distributions, is less sensitive to this absolute normalization. This is the reason we exclude the data of other groups (lower part of Table IV) from the present averaging procedure (last row in Table IV). We note that, deformation, which is important in some p -shell nuclei, is not included in any way in our calculations, due to the use of spherical Hartree-Fock density distributions.

Further, we checked to see to what extent the double folding potentials, renormalized to fit the elastic scattering data, give the same results as the phenomenological potentials when used to calculate the cross sections for the proton transfer reactions. For the reaction ${}^9\text{Be}({}^{10}\text{B}, {}^9\text{Be}){}^{10}\text{B}$ we found that the cross section calculated with the JLM(1) potential, renormalized as above, differs by less than 1% (integral over the angles from 0° to 45°) from that calculated using the phenomenological potential 1. Furthermore, the double folding potential used has the same volume integrals as the phenomenological potential 1. In Ref. [15] we left open the choice of the potential we use to extract the value of the ANC for the system ${}^9\text{Be}+p \rightarrow {}^{10}\text{B}$, and two slightly different

values were extracted using potentials 1 and 2. The present study and the calculations made with the double folding potential indicate that we can select potential 1 as the only potential, and that the value $C_1^2 = 4.91(37) \text{ fm}^{-1}$ is a better choice than the weighted average $C^2 = 5.06(46) \text{ fm}^{-1}$ given previously. For the reaction ${}^{13}\text{C}({}^{14}\text{N}, {}^{13}\text{C}){}^{14}\text{N}$ we found that the value of the cross section calculated using the double folding potential JLM(1) varies at any angle between $\theta_{\text{c.m.}} = 0^\circ - 35^\circ$ by less than 2% from that calculated using potential 1 in Table II, and its integral over the same angular range does not vary at all. This is easy to understand given the fact that the surface part of the nuclear potential is the contributing factor in the description of both the elastic scattering and the transfer reaction. Previously we found that the calculated cross sections for the proton transfer reaction ${}^{13}\text{C}({}^{14}\text{N}, {}^{13}\text{C}){}^{14}\text{N}$ differ by about 2% between any consecutive phenomenological potential families in Table II, as described in Ref. [16]. The present verification increases our confidence in using the double folding procedure for the description of the transfer reactions.

VI. OPTICAL POTENTIALS FOR ${}^{10}\text{B}({}^7\text{Be}, {}^8\text{B}){}^9\text{Be}$ AND ${}^{14}\text{N}({}^7\text{Be}, {}^8\text{B}){}^{13}\text{C}$ REACTIONS

Using the procedure outlined above, the JLM(1) effective nucleon-nucleon interaction and the average renormalization coefficients extracted, we calculated the optical model potentials needed in the analysis of the proton transfer reactions ${}^{10}\text{B}({}^7\text{Be}, {}^8\text{B}){}^9\text{Be}$ and ${}^{14}\text{N}({}^7\text{Be}, {}^8\text{B}){}^{13}\text{C}$ at $E({}^7\text{Be}) = 84 \text{ MeV}$, which were the original motivation for the present study. The systems involve the radioactive ${}^7\text{Be}$ and ${}^8\text{B}$ nuclei, both loosely bound and with important clusterization in their ground states. This made us treat the Hartree-Fock densities carefully, forcing the calculations to reproduce the correct binding energies through slight modifications in the surface term as stated before. Furthermore, in the final calculations we imposed self-consistency by requiring that the tail of the density distribution of ${}^8\text{B}$ have the asymptotic behavior given by the ANC extracted from the transfer reaction (but not predicted by HF). This produced changes in the potentials only at distances larger than 8 fm, as shown in Fig. 8, and did not introduce any substantial change in the calculated proton transfer cross sections. The optical model potentials obtained reproduced very well the measured angular distributions for the elastic scattering of ${}^7\text{Be}$ on the ${}^{10}\text{B}$ (Ref. [4]) and ${}^{14}\text{N}$ (Ref. [5]) targets without any need for further adjustments [in both cases elastic scattering was actually calculated using JLM(1) potentials not only on the main component of the target, ${}^{10}\text{B}$ and ${}^{14}\text{N}$, respectively, but also on the ${}^{16}\text{O}$ and ${}^{12}\text{C}$ nuclei present as impurities in the ${}^{10}\text{B}$ and in the melamine target, respectively]. This provided confidence for using the extracted potentials for the description of the angular distributions of the proton transfer reactions. Again, the shape of the measured angular distributions are very well reproduced, as seen for ${}^{14}\text{N}({}^7\text{Be}, {}^8\text{B}){}^{13}\text{C}$ in Fig. 9. In turn, the calculated cross sections were used to extract the asymptotic normalization coefficient for the system ${}^8\text{B} \rightarrow {}^7\text{Be}+p$ and, consequently, the astrophysical factor $S_{17}(0)$ reported in Refs. [4,5]. The potentials obtained for these

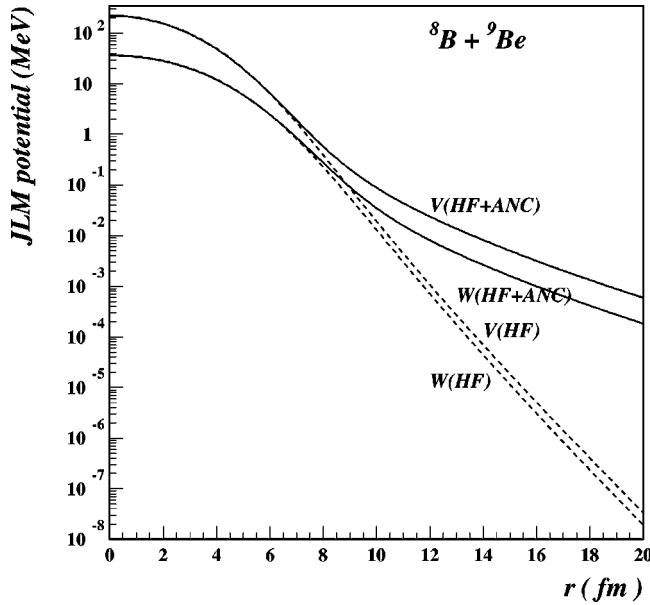


FIG. 8. The double folded potentials calculated with the standard Hartree-Fock mass distributions (dashed lines) are compared with those obtained when the tail of the proton distribution of ${}^8\text{B}$ is given by the ANC obtained from our experiments (full line). Both real (V) and imaginary (W) potentials are shown for the system ${}^8\text{B}+{}^9\text{Be}$, using the JLM(1) effective interaction.

nucleus-nucleus combinations involving radioactive ${}^7\text{Be}$ and ${}^8\text{B}$ are not exactly of Woods-Saxon shape, but can be approximated in the region of their surface by Woods-Saxon potentials. In Table V we give the parameters found by fitting the range of radii $r=2-12$ fm.

In order to estimate the uncertainty in the ANCs due to the optical model potentials, we consider that the standard deviations of the normalization coefficients $\delta N_V=0.014$ and $\delta N_W=0.087$ give a good measure of the uncertainty with which we can find the depths of the real and imaginary potentials wells, respectively. By the choice of the systems considered here, we span a good range of p -shell nuclei, averaging properties similar to those of radioactive ones in terms of mass, separation energy, structure of the ground states, incident energies, number of open reaction channels, etc. We used these standard deviations around the average value of the renormalization coefficients to evaluate the uncertainty in extracting the ANCs. The uncertainties arise through the DWBA calculations of the transfer reaction cross section. We took the geometry as given by the double folding procedure and determined the variation of the calculated proton transfer cross section integrated over the angular range relevant in the experiments. The potential depths were varied from $N_V - \delta N_V$ to $N_V + \delta N_V$ for the real part and from $N_W - \delta N_W$ to $N_W + \delta N_W$ for the imaginary part for the entrance and exit channels independently and the resulting variations were added in quadrature to estimate the relative uncertainty in the DWBA calculations. With this procedure we found a 7.5% uncertainty in the calculated ${}^{10}\text{B}({}^7\text{Be}, {}^8\text{B}){}^9\text{Be}$ transfer cross section due to DWBA calculations. The same procedure gave an estimate of 7.7% for the uncertainty due to

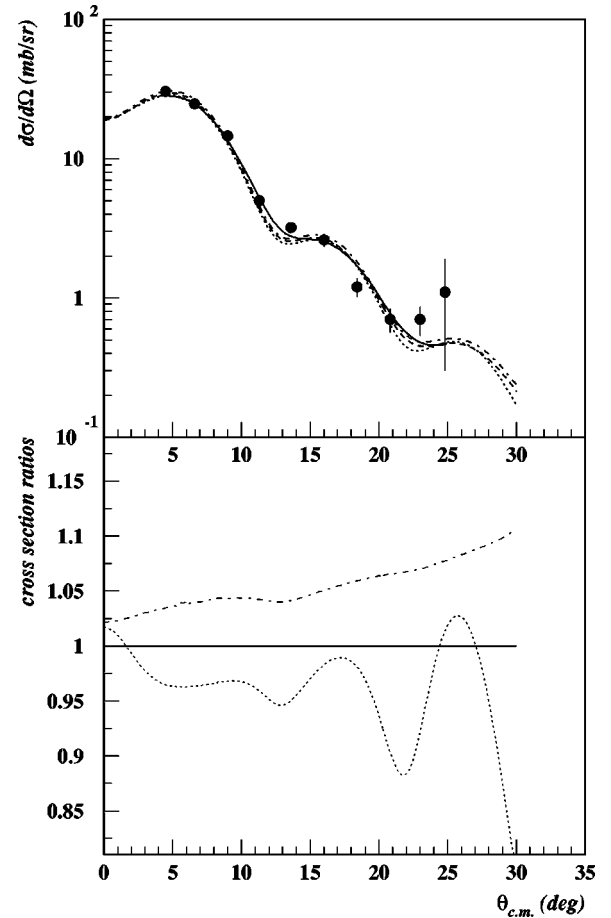


FIG. 9. The angular distribution for the elastic proton transfer ${}^{14}\text{N}({}^7\text{Be}, {}^8\text{B}){}^{13}\text{C}$ at $E_{\text{lab}}=84$ MeV, calculated using the optical model potential obtained with the JLM(1) effective interaction (dashed line) is compared with the one smoothed by a Monte Carlo procedure to account for the experimental resolution (solid line) and with the experimental points. The dotted and dash-dotted lines represent the calculated cross section (not smoothed) with the imaginary potential depths renormalized by $N_W \pm \delta N_W$ (upper panel). The lower panel presents the ratios of the transfer cross sections calculated using renormalization coefficients for the imaginary part of the potential $N_W + \delta N_W$ (dotted line), N_W (solid line), and $N_W - \delta N_W$ (dash-dotted line) to that calculated with the median value N_W .

DWBA calculations for the ${}^{14}\text{N}({}^7\text{Be}, {}^8\text{B}){}^{13}\text{C}$ reaction. In both cases most of the contribution comes from the uncertainty in the imaginary renormalization coefficient (7.5%), while the real one contributes only about a quarter of that (2%). Note that in varying separately the depths of the potentials in the entrance and exit channels for the same reaction, we treat the uncertainties as uncorrelated between the channels involving ${}^7\text{Be}$ and ${}^8\text{B}$, respectively, whereas the uncertainties between the two different reactions remain correlated through the use of the same procedure and of the same average values for the renormalization coefficients. When we treated the uncertainties in assessing the depths of the potentials in the entrance and exit channels as totally correlated, as we did in Ref. [4], we obtained an uncertainty of about 10%.

TABLE V. Parameters of volume Woods-Saxon type potentials that best fit the nuclear part of the numerical potentials obtained with the double folding procedure using the JLM(1) effective interaction in the range $r=2-12$ fm (see text). Renormalization of the depths is included. R_V and R_W are the half-radii of the potentials.

Projectile-target	E_{inc} [MeV]	V [MeV]	W [MeV]	R_V [fm]	R_W [fm]	a_V [fm]	a_W [fm]	J_V [MeV fm ³]	J_W [MeV fm ³]
${}^7\text{Be}+{}^{10}\text{B}$	84	63.8	29.4	3.18	3.49	0.85	0.95	210	130
${}^8\text{B}+{}^9\text{Be}$	81	67.0	31.8	3.18	3.54	0.88	0.99	236	145
${}^7\text{Be}+{}^{14}\text{N}$	84	79.1	36.0	3.30	3.62	0.88	0.98	207	126
${}^8\text{B}+{}^{13}\text{C}$	78	85.2	39.3	3.30	3.76	0.91	1.02	216	145

We note here that given the observed strong dependence of the calculations on the imaginary part of the potential, and the relative independence of the real and imaginary parts of the potential, the measurement of the total reaction cross section of ${}^7\text{Be}$ and ${}^8\text{B}$ might be useful. It can set an extra constraint on the renormalization of the imaginary part of the potential, and eventually decrease the uncertainty in the potential used, and therefore in the DWBA results. With ${}^7\text{Be}$ such experiments may be feasible, but given the present difficulties in obtaining good intensities for ${}^8\text{B}$, those may only be possible on Si targets in experiments similar to those reported in Ref. [46]. A comparison between the total reaction cross sections measured in these experiments and those predicted with a renormalized imaginary potential calculated as above, would be useful to recheck the whole procedure. In addition, elastic scattering data for ${}^8\text{B}$ on p -shell nuclei at around 10 MeV/nucleon would be extremely useful for verifying our approach. Unfortunately, the intensity of the ${}^8\text{B}$ beams is too small at present to make these measurements feasible.

VII. CONCLUSIONS

We have measured the elastic scattering of ${}^7\text{Li}$, ${}^{10}\text{B}$, ${}^{13}\text{C}$, and ${}^{14}\text{N}$ on ${}^9\text{Be}$ and ${}^{13}\text{C}$ targets at or around $E/A = 10$ MeV/nucleon for angular ranges up to around the nuclear rainbow angle, using a fine angle binning of $\Delta\theta_{\text{lab}} = 0.5^\circ$. All these projectile-target combinations, with the exception of ${}^{14}\text{N}+{}^{13}\text{C}$, have in common the fact that one or both partners are weakly bound and we expect contributions from break-up channels to be important. At the same time it is known that at energies around 10 MeV/nucleon the contribution of the dynamic polarization potential is non-negligible. Parameters for optical model potentials of Woods-Saxon form were obtained from the fit of the elastic scattering angular distributions. In addition, nucleus-nucleus potentials were calculated by a double folding procedure using six different effective nucleon-nucleon interactions. The nuclear densities calculated for each partner in the Hartree-Fock approximation were folded with four different versions of the M3Y nucleon-nucleon interaction and with the effective interaction of Jeukenne *et al.* [11], calculated with two different techniques to account for the local density. The resulting nucleus-nucleus potentials were later renormalized to obtain a fit of the elastic scattering data. The normalization constants have similar values in all systems for each effective

interaction used, which makes it appear likely that the procedure can be extended to the calculation of optical potentials for other similar nucleus-nucleus systems. Similar conclusions about the validity of the use of folding models were reached in previous works (see, e.g., Ref. [44], and references therein). However, we note that understanding reactions involving halo nuclei has been more challenging (Refs. [44,45], and references therein). We may not have sufficient data at present to determine if the present mean field approach, and especially the value of the renormalization coefficients, have more than a local validity.

From all effective interactions used, we conclude that JLM(1) gives the best results. It provides us with an imaginary part that has a geometry which is independent from that of the real part of the potential. The imaginary well produced is wider than the real one, as the fit of the data with phenomenological Woods-Saxon wells requires. At the same time, it gives the least spread in the value of the renormalization coefficients, which suggests that its density dependence accounts very well for the differences between the nuclei involved, particularly in the surface region. We find that while the depth of the real potential needs a substantial renormalization ($\langle N_V \rangle = 0.366 \pm 0.014$), the imaginary part needs no such renormalization ($\langle N_W \rangle = 1.000 \pm 0.087$). This also suggests that the imaginary part of the effective interaction is well accounted for. The need for a substantial renormalization of the real part was attributed to the effect of the break-up channels, which are very important in nuclei with low binding energies similar to those encountered in our experiments [34]. This suggests that the average value of the renormalization constant for the real potential depth found above is valid for the region of p -shell nuclei considered in this study and might be somewhat different in other regions.

The renormalized double folded potentials obtained were also used in the DWBA analysis of the proton transfer reactions with stable nuclei, and the results were found to be in excellent agreement with those given by the phenomenological Woods-Saxon potentials. We found that comparison of the double folded potentials and the phenomenological ones gives a way to select between the different families based on their volume integrals.

Finally, the procedure found was applied to extract the optical model potentials for the ${}^7\text{Be}$ and ${}^8\text{B}$ radioactive projectiles needed in the description of the ${}^7\text{Be}+{}^{10}\text{B}$ and ${}^7\text{Be}+{}^{14}\text{N}$ experiments. Good description for the elastic scatter-

ing data is found without any need for readjustment of the shape or magnitude of the angular distributions. The shape of the angular distributions measured for the proton transfer reactions $^{10}\text{B}(^7\text{Be}, ^8\text{B})^9\text{Be}$ and $^{14}\text{N}(^7\text{Be}, ^8\text{B})^{13}\text{C}$ are also very well predicted. The calculated DWBA cross sections were used to extract the ANC for the $^8\text{B} \rightarrow ^7\text{Be} + p$ system from each reaction, and consequently the astrophysical $S_{17}(0)$ factor reported in Refs. [4,5]. Furthermore, we used the standard deviations of the renormalization coefficients δN_V , δN_W to estimate the contribution of the DWBA calculations to the

uncertainty of the determined ANC and thus $S_{17}(0)$. We found this contribution to be around 8%.

ACKNOWLEDGMENTS

One of us (F.C.) acknowledges the support of the Cyclotron Institute, Texas A&M University, for a stay in College Station, TX, during which a part of this work was done. This work was supported in part by the U. S. Department of Energy under Grant No. DE-FG03-93ER40773 and by the Robert A. Welch Foundation.

-
- [1] H. M. Xu, C. A. Gagliardi, R. E. Tribble, A. M. Mukhamedzhanov, and N. K. Timofeyuk, *Phys. Rev. Lett.* **73**, 2027 (1994).
- [2] C. A. Gagliardi, R. E. Tribble, J. Jiang, A. M. Mukhamedzhanov, L. Trache, H. M. Xu, S. J. Yennello, and X. G. Zhou, *Nucl. Phys.* **A588**, 327c (1995).
- [3] J. G. Ross, G. Goerres, C. Iliadis, S. Vouzoukas, M. Wiescher, R. B. Vogelaar, S. Utku, N. P. T. Batteman, and P. D. Parker, *Phys. Rev. C* **52**, 1681 (1995).
- [4] A. Azhari, V. Burjan, F. Carstoiu, H. Dejbakhsh, C. A. Gagliardi, V. Kroha, A. M. Mukhamedzhanov, L. Trache, and R. E. Tribble, *Phys. Rev. Lett.* **82**, 3960 (1999).
- [5] A. Azhari, V. Burjan, F. Carstoiu, C. A. Gagliardi, V. Kroha, A. M. Mukhamedzhanov, X. D. Tang, L. Trache, and R. E. Tribble, *Phys. Rev. C* **60**, 055803 (1999).
- [6] W. Liu *et al.*, *Phys. Rev. Lett.* **77**, 611 (1996).
- [7] C. Powell, D. J. Morrissey, D. W. Anthony, B. Davids, M. Fauerbach, P. F. Mantica, B. M. Sherrill, and M. Steiner, in *Proceedings of the Second International Conference on Exotic Nuclei and Atomic Masses*, ENAM98, edited by B. M. Sherrill, D. J. Morrissey, and C. N. Davids, AIP Conf. Proc. No. 455 (AIP, New York, 1998), p. 908.
- [8] C. A. Gagliardi, A. M. Mukhamedzhanov, R. E. Tribble, and H. M. Xu, *Phys. Rev. Lett.* **80**, 421 (1998).
- [9] J. C. Fernandes, R. Crespo, F. M. Nunes, and I. J. Thompson, *Phys. Rev. C* **59**, 2865 (1999).
- [10] Dao T. Khoa and W. von Oertzen, *Phys. Lett. B* **342**, 6 (1995).
- [11] J. P. Jeukenne, A. Lejeune, and C. Mahaux, *Phys. Rev. C* **16**, 80 (1977).
- [12] M. Beiner and R. J. Lombard, *Ann. Phys. (N.Y.)* **86**, 262 (1974); F. Carstoiu and R. J. Lombard, *ibid.* **217**, 279 (1992).
- [13] E. O. Alt and W. Sandhas, in *Coulomb Interactions in Nuclear and Atomic Few-Body Collisions*, edited by F. S. Levin and D. Micha (Plenum Press, New York, 1996), p. 1.
- [14] J. S. Al-Khalili and J. A. Tostevin, *Phys. Rev. Lett.* **76**, 3903 (1996); J. S. Al-Khalili, J. A. Tostevin, and I. J. Thompson, *Phys. Rev. C* **54**, 1843 (1996).
- [15] A. M. Mukhamedzhanov, R. E. Tribble, C. A. Gagliardi, H. L. Clark, Y.-W. Lui, L. Trache, H. M. Xu, and J. Cejpek, *Phys. Rev. C* **56**, 1302 (1997).
- [16] L. Trache, H. L. Clark, C. A. Gagliardi, Y.-W. Lui, A. M. Mukhamedzhanov, R. E. Tribble, and F. Carstoiu, *Phys. Rev. C* **58**, 2715 (1998).
- [17] D. M. Pringle, W. N. Catford, J. S. Winfield, D. G. Lewis, N. A. Jelley, K. W. Allen, and J. H. Coupland, *Nucl. Instrum. Methods Phys. Res. A* **245**, 230 (1986).
- [18] D. H. Youngblood and J. B. Bronson, *Nucl. Instrum. Methods Phys. Res. A* **361**, 37 (1995).
- [19] D. H. Youngblood, Y.-W. Lui, H. L. Clark, P. Oliver, and G. Simler, *Nucl. Instrum. Methods Phys. Res. A* **361**, 539 (1995).
- [20] S. Kowalski and H. A. Enge, computer code RAYTRACE, 1986 (unpublished).
- [21] F. Carstoiu, code OPTIMINIX (unpublished).
- [22] M. Rhoades-Brown, M. McFarlane, and Steven Pieper, *Phys. Rev. C* **21**, 2417 (1980); **21**, 2436 (1980).
- [23] J. Raynal, *Phys. Rev. C* **23**, 2571 (1981).
- [24] G. Igo, *Phys. Rev.* **115**, 1665 (1959).
- [25] G. R. Satchler and W. G. Love, *Phys. Rep.* **55**, 183 (1979).
- [26] D. E. DiGregorio, J. Gomez del Campo, Y. D. Chan, J. L. C. Ford, Jr., D. Shapira, and M. E. Ortiz, *Phys. Rev. C* **26**, 1490 (1982).
- [27] J. Cook, H. J. Gils, H. Rebel, Z. Majka, and H. Klewe-Nebenius, *Nucl. Phys.* **A388**, 173 (1982).
- [28] H. J. Gils, H. Rebel, and E. Friedman, *Phys. Rev. C* **29**, 1295 (1984).
- [29] H. de Vries, C. W. de Jager, and C. de Vries, *At. Data Nucl. Data Tables* **36**, 495 (1987).
- [30] G. Audi and A. H. Wapstra, *Nucl. Phys.* **A565**, 66 (1993).
- [31] I. Tanihata, H. Hamagaki, O. Hashimoto, Y. Shida, N. Yoshikawa, K. Sugimoto, O. Yamakawa, T. Kobayashi, and N. Takahashi, *Phys. Rev. Lett.* **55**, 2676 (1985); I. Tanihata, T. Kobayashi, O. Yamakawa, T. Shimoura, K. Ekuni, K. Sugimoto, N. Takahashi, T. Shimoda, and H. Sato, *Phys. Lett. B* **206**, 592 (1988).
- [32] T. Hoshino, H. Sagawa, and A. Arima, *Nucl. Phys.* **A596**, 271 (1990).
- [33] G. Bertsch, J. Borysowicz, H. McManus, and W. G. Love, *Nucl. Phys.* **A284**, 399 (1977).
- [34] G. R. Satchler and Dao T. Khoa, *Phys. Rev. C* **55**, 285 (1997).
- [35] D. H. Youngblood, H. L. Clark, and Y.-W. Lui, *Phys. Rev. Lett.* **82**, 691 (1999).
- [36] E. Bauge, J. P. Delaroche, and M. Girod, *Phys. Rev. C* **58**, 1118 (1998).
- [37] X. Campi and D. W. L. Sprung, *Nucl. Phys.* **A194**, 401 (1972).
- [38] A. M. Kobos, B. A. Brown, P. E. Hodgson, G. R. Satchler, and A. Budzanowski, *Nucl. Phys.* **A384**, 65 (1982); A. M. Kobos, B. A. Brown, R. Lindsay, and G. R. Satchler, *ibid.* **A425**, 205 (1984).
- [39] G. R. Satchler, *Phys. Lett.* **83B**, 284 (1979).

- [40] Y. Sakuragi, Phys. Rev. C **35**, 2161 (1987).
- [41] P. Schwandt, W. W. Jacobs, M. D. Kaitchuck, W. D. Ploughe, F. D. Becchetti, and J. Jäneke, Phys. Rev. C **24**, 1522 (1981).
- [42] F. Carstoiu and M. Lassaut, Nucl. Phys. **A597**, 269 (1996).
- [43] A. F. Zeller, Y.-W. Lui, R. E. Tribble, and D. M. Tanner, Phys. Rev. C **22**, 1534 (1980).
- [44] M. E. Brandan and G. R. Satchler, Phys. Rep. **285**, 143 (1997).
- [45] R. Crespo and R. C. Johnson, Phys. Rev. C **60**, 034007 (1999).
- [46] R. E. Warner *et al.*, Phys. Rev. C **54**, 1700 (1996); Nucl. Phys. **A635**, 292 (1998), and references therein.